3D printing of composite scaffolds based on polycaprolactone matrix reinforced with monticellite and akermanite for bone repair; mechanical and biological properties

MTLA 34 (2024) 102057

Contents lists available at ScienceDirect

Materialia

journal homepage: www.elsevier.com/locate/mtla

Full Length Article

3D printing of composite scaffolds based on polycaprolactone matrix reinforced with monticellite and akermanite for bone repair; mechanical and biological properties

Alma Kalali [a], Hamidreza Rezaie [a,*], Saeed Hesaraki [b], Mohammad Khodaei [c], Farzaneh Teimoory [a], Abdollah Saboori [d,*]

[a] School of Metallurgy and Materials Engineering, Iran University of Science and Technology, Tehran, Iran
[b] Nanotechnology and Advanced Materials Department, Materials and Energy Research Center, Karaj, Alborz, Iran
[c] Department of Materials Science and Engineering, Golpayegan University of Technology, Golpayegan, Iran
[d] Integrated Additive Manufacturing Center, Department of Management and Production Engineering, Politecnico di Torino, Torino, Italy

ARTICLE INFO

Keywords:
3D printing
Scaffold
Akermanite
Monticellite
Sol-gel

ABSTRACT

This investigation examines the bioactivity and mechanical properties of composite scaffolds made from polycaprolactone (PCL) and augmented with akermanite ($Ca_2MgSi_2O_7$) (AK) and monticellite ($CaMgSiO_4$) (MNT) powders synthesized via the sol-gel method. The study systematically assesses the impact of varying proportions of the AK and MNT admixture, specifically at 10, 15, and 20 wt.% of the total composite weight. Morphological characterization of the powders is conducted. The composite scaffolds are fabricated using 3D printing. Scanning electron microscopy (SEM) images show interconnected and open-pore structures. Mechanical testing results indicate an increase in compressive strength facilitated by the AK and MNT bioceramics. The scaffold made of PCL and containing 15 wt.% nanopowders of AK/MNT exhibits superior compressive strength, measuring at 14.2 ± 0.84 MPa compared to other scaffolds. Bioactivity assessments confirm that the composite scaffolds can form apatite in simulated body fluid. The outcomes collectively demonstrate the effectiveness of the bioactive 3D-printed scaffolds, which have improved mechanical properties, confirming their suitability for use in cancellous bone repair.

1. Introduction

Bone is a connective tissue containing four cell types: osteoblasts, osteocytes, osteoclasts, and bone lining cells [1]. It serves as a strong structural element in the human body, providing support and protection to various anatomical regions while also allowing for flexibility [2]. The incidence of bone disorders, including displacements, scoliosis, osteoporosis, bone defects or tumors, congenital anomalies, and osteoarthritis, has increased. In response to these challenges, advancements in medical therapeutics have been made, and many methods have been employed over the years to address various bone ailments [3]. Bone repair has many challenges, but bone tissue engineering is the most suitable technique for improving bone defects with biocompatible materials [4].

Inorganic bioceramics, calcium phosphate ceramics like hydroxyapatite (HA), biphasic calcium phosphate (BCP), and β-tricalcium phosphate are applied for bone functions because their chemical formulation is similar to natural bone. These calcium phosphate ceramics have been extensively used in clinics as bone replacement materials [5]. Also, calcium phosphate ceramics have good biological properties like bioactivity and osteoconductivity [6].

Still, the shortcomings of three calcium phosphate (TCP) ceramics are the poor mechanical properties, such as low fracture toughness and compressive stability and high absorption rate [5,7,8]. Therefore, bioactive silicate ceramics are a sufficient choice for remodelling bone because of their augmented mechanical properties compared to HA and regulated degradation rate. Besides, the existence of Mg^{2+}, Ca^{2+}, and Si^{4+} ions leads to enhanced cell adhesion and stimulates osteoblast cell growth [6,9].

Calcium silicate bioceramics include Monticellite ($CaMgSiO_4$) (MNT), Akermanite ($Ca_2MgSi_2O_7$) (AK), and diopside ($CaMgSi_2O_6$). Chen et al. [10]. declared that MNT has apatite-formation ability after

* Corresponding author.
E-mail addresses: hrezaie@iust.ac.ir (H. Rezaie), abdollah.saboori@polito.it (A. Saboori).

https://doi.org/10.1016/j.mtla.2024.102057
Received 29 January 2024; Accepted 8 March 2024
Available online 9 March 2024

immersion in simulated body fluid (SBF) and can increase osteoblast growth. AK is attractive for biomedical applications, and it has also been demonstrated in both in-vitro and in-*vivo* cell augmentation conditions compared with β-TCP [11].

Accordingly, AK is degradable and reveals apatite-formation in SBF [12]. Moreover, AK is a bioactive bioceramic and it can stimulate the proliferation and differentiation of bone marrow-derived stem cells [13]. Due to its similarity to bone tissue and enhancement of mechanical properties, Ak bioceramic is a suitable candidate for orthopaedic applications [14].

As well as in the CaO-MgO-SiO_2 system, MgO content influences mechanical properties and apatite-formation ability. In a case with an enhanced MgO content, mechanical strength and crystal structure were refined due to the higher bond energy of Mg-O compared to the Ca-O one. Additionally, the crystal structures of MNT and AK are different; AK and MNT have tetragonal and trimetric structures, respectively [10, 15].

MNT and AK powders have been synthesized using different methods; one of the most well-known is sol-gel [9]. Overall, the sol-gel method has been recognized for its ability to control the shape and size of nanoparticles, making it a valuable tool in the field of nanotechnology. Sol-gel is the most uncomplicated method to prepare various ceramic nanoparticles [16].

This process involves the formation of a gel-like substance, or "gel", from a liquid solution, followed by removing the solvent to form a solid, or "gel". The sol-gel process is often used to produce ceramics and other materials due to its ability to create nanoparticles with a high surface area [17]. For instance, the sol-gel technique was successfully used to produce MNT powder at a temperature of 780 °C for 2 h, resulting in the formation of nanoparticles [18]. Hou et al. [19]. prepared AK powders at 1350° C for 4 h by sol-gel method. In another research, Wu et al. [20] synthesized AK powders via the sol-gel method at 1300° C for 3 h.

Also, AK powders was synthesized by sol-gel method at 1300° C for 2 h [21]. Likewise, for the sol-gel process, the calcination temperature is lower than that of solid reaction techniques [22]. It is well documented that ceramics are brittle and have low fracture toughness. To address these issues, polymers can be prepared to increase flexibility, fracture toughness, and moderate biodegradability [12].

Polycaprolactone (PCL), which is a synthesized polymer with molecular formula $(C_6H_{10}O_2)_n$ has biocompatible and biodegradable properties, is a semicrystalline polyester with a low melting point (T_m = 60° C) [23]. The PCL polymer has remarkable properties such as mechanical flexibility and convenient processability [24]. It is used for fabricating tissue engineering scaffolds and drug delivery applications. One of the most important features of synthesized polymers is producing complex geometries with significant elongation [25].

However, to overcome weaknesses such as low bioactivity, hydrophobicity, and lack of osteogenic capability, synthesized polymer and bioceramic particles are considered [26].

The goal of tissue engineering is to achieve optimal biological and mechanical performance for tissue regeneration. In bone tissue engineering, scaffolds serve as a platform for cell attachment, proliferation, and vascular ingrowth. Scaffolds must have a construct with interconnected pores and adequate surface topography [27,28]. In recent years, 3D printing has been used for manufacturing tissue engineering scaffolds [26]. This method allows for the creation of intricate shapes through a layer-by-layer process. The benefits of 3D printing include the ability to computationally design structures, increased portability, and greater precision compared to traditional techniques [29]. One of these advanced methods is fused deposition modelling (FDM), which involves the melting of thermoplastic polymers such as poly (lactic acid) (PLA), polycarbonate, and acrylonitrile-butadiene-styrene (ABS) [30] into filaments or granules. The liquid material is then extruded from a nozzle and solidifies rapidly on the sheet [31]. FDM is a popular and cost-effective rapid prototyping method due to its high acceleration print [32]. This method involves constructing a model using 3D graphic software capable of exporting STL files. Interconnected porous construction is principal for tissue engineering functions because of the ingrowth of new tissue into scaffolds. Furthermore, the size of pores should be more extensive than 150 μm to develop vascularization [33]. This study presents a novel material for bone tissue engineering that involves the combination of MNT and AK powders with a biodegradable polymer. The study utilizes advanced 3D printing to create composite scaffolds that overcome traditional challenges such as poor mechanical properties. The integration of MNT and AK enhances the scaffold's performance, addressing the complexities of bone repair. This study represents progress towards achieving optimal biological and mechanical outcomes for tissue regeneration in the field of bone engineering.

2. Materials and methods

2.1. Materials

The materials used in this study were PCL (80,000 Molecular Weight, granule, ESUN, South Korea), Magnesium chloride hexahydrate ($MgCl_2{\cdot}6H_2O$, purity: 99 %, China Grade), calcium nitrate tetrahydrate ($Ca(NO_3)_2{\cdot}4H_2O$, purity: 99 %, China Grade), colloidal silica (30% W/V SiO_2, purity: 99,8 %, Sigma-Aldrich), distilled water and nitric acid (HNO_3, purity: 98 %, Merck, Germany), simulated body fluid (SBF, Nick Ceram Razi.Co./Iran), phosphate buffered saline (PBS, pH= 7.4, Sigma-Aldrich), 3-(4,5- dimethylthiazol-2-yl) −2,5-diphenyltetrazolium-bromide (MTT, Sigma-Aldrich/USA), MG-63 osteosarcoma cell line (Cell Bank of Pasteur Institute/Iran), fetal bovine serum (FBS, Viva cell, USA), dimethyl sulfoxide (DMSO, Bioidea, Iran) Dulbecco's Modified Eagle Medium (DMEM, Vivacell, USA) and chloroform (CHCl3, Merck, Germany).

2.2. Synthesis of AK and MNT powders

The MNT and AK powders were synthesized using a sol-gel process. First, $MgCl_2{\cdot}6H_2O$ and $Ca(NO_3)_2{\cdot}4H_2O$ were added to the distilled water while the powders were dissolving completely on the stirrer. Then, the SiO_2 solution and a small amount of nitric acid were added, while the pH of the solution was measured, and the gel was formed. Afterwards, the gel was dried at 110° C for 2 days in an oven.

In order to estimate the calcination temperature, the dried gel was evaluated by simultaneous thermal analysis (STA). After calcination at 1000° C for 2 h and 1300° C for 1 h in air, MNT and AK powders were synthesised, respectively. The dry powders were ground in an agate mortar pestle and sieved to 250 mesh. Mechanical milling was employed to crush the powders and refine their particle size reduction, wherein the powders underwent ball milling via a planetary ball mill with dual compartments (Sanat Ceram Company, Iran) for 3 h. The material of the cup and balls was zirconia. The disc rotation speed during milling was set at 300 rpm, and a ball-to-powder weight ratio of 20:1 was maintained. Subsequently, the milled powders were sieved using a 400-mesh sieve.

2.3. Preparation of AK/MNT/PCL scaffolds

The scaffolds were fabricated employing a 3D-printing methodology, as illustrated in Fig. 1. Various proportions of the AK and MNT mixture, namely 10, 15, and 20 wt.% of the total composite weight, were incorporated into the PCL polymer matrix. The weight ratios of AK and MNT in the mixture were maintained at 50:50. To elaborate, PCL granules were dissolved in 50 cc chloroform under a stirring speed of 200 rpm until a homogeneous solution was attained. Simultaneously, powders were gradually introduced into the solution and stirred for a duration of 2 h. Subsequently, a uniform polymer/ceramic suspension was achieved. The composite material was shaped into porous scaffolds utilizing a fused deposition modelling (FDM) 3D printer system (3D bioprinter: Chakad, CSS1, Iran).

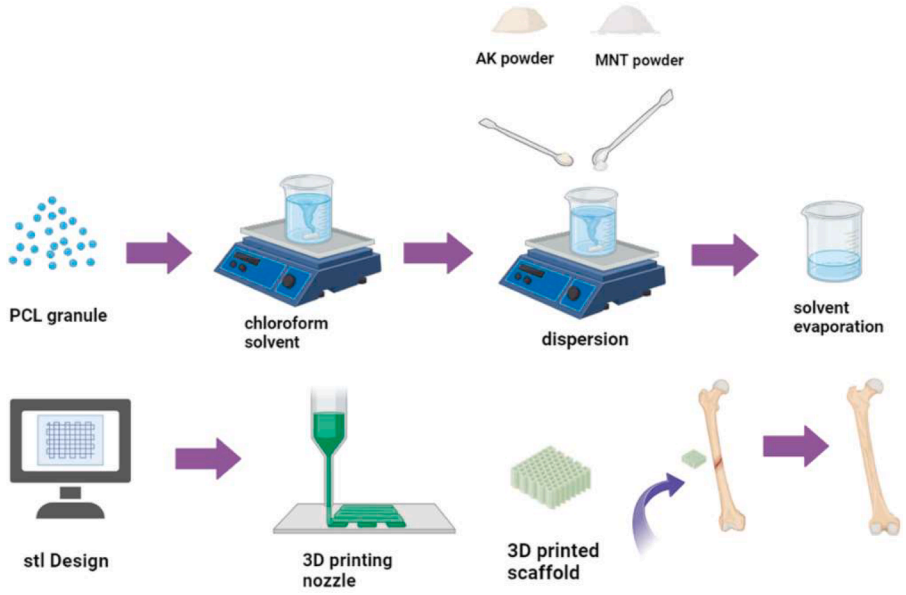

Fig. 1. The schematic illustration of the preparation of porous scaffold.

The determining features for producing scaffolds by the FDM technique are described in Table 1.

2.4. Characterization

The morphology of AK and MNT powders was assessed using transmission electron microscopy (TEM). The powders were dispersed in ethanol and sonicated to create a diluted homogeneous suspension. A small volume of the suspension was then deposited onto carbon-coated copper grids. The morphology of AK and MNT particles was characterized utilizing a TEM apparatus (GM200 PEG Philips) operating at a voltage of 200 kV. The analysis of particle size distribution and determination of average particle size for the powders were accomplished through microstructural image processing (MIP) software, which is used to analyze metallographic and microscopic images.

Chemical bonds were investigated using Fourier transform infrared spectroscopy (FTIR). The infrared spectra were acquired from the surfaces of the scaffolds using a spectrometer (Spectrum Two models; Perkin Elmer) within the range of 400–4000 cm^{-1}.

For the determination of the phase composition of the synthesized AK and MNT powders, x-ray diffraction (XRD) analysis was employed. The diffraction data were collected using a Cu-Kα radiated diffractometer (D8 Advance, Bruker Kanagawa Japan) operating at 20 kV and 10 mA.

The morphological characteristics of the scaffolds were examined through scanning electron microscopy (SEM, TESCAN, Brno, Czech Republic). In preparation for SEM evaluation, the surfaces of the samples were coated with Ag. The thickness diameter and pore size of the scaffolds were quantified using MIP software. Furthermore, elemental image analysis was conducted through MAP and EDS techniques integrated with the SEM instrument.

The porosity of the composite scaffolds consisting of AK/MNT/PCL was quantified through the liquid displacement technique, employing the Archimedes method for porosity estimation.

Initially, the dry weight of the scaffolds was determined. Subsequently, the scaffolds were immersed in distilled water until saturation, facilitating the absorption of distilled water. Following saturation, the scaffolds were reweighed to ascertain the final weight. Likewise, the liquid displacement method was used to evaluate the porosity (p) following Eq. (1).

$$P = \frac{W_2 - W_1}{W_2 - W_3} \times 100 \quad (1)$$

Where W_1 is the weight of the dry scaffold in air, W_2 is the weight of the wet scaffold, and W_3 is the weight of the scaffold after it is soaked in distilled water until it is saturated [34].

For the mechanical testing, scaffolds were fabricated with cross-sectional dimensions of 10 × 10 mm^2. Load-displacement data were acquired using Jinan testing equipment from China. Subsequently, stress-strain curves were generated, and the compressive strength and elastic modulus were determined.

Samples with dimensions of 10 × 10 × 5 mm^3 were then prepared and immersed in SBF at 37 °C for 28 days. Scaffolds underwent SBF immersion for both 7 and 28 days. Upon completion of the immersion periods, the scaffolds were retrieved from the SBF solution, washed with distilled water, and dried for 2 days at room temperature. The surface morphology of the samples was examined through SEM. The chemical bonds were also analyzed using FTIR according to a previously established methodology. The MG-63 cell line was employed for assessing cytotoxicity and cell adhesion. Initially, a seeding density of 1 × 10^4 cells was cultured on sterilized scaffolds with DMEM, supplemented with 10 μL FBS, and incubated at 37 °C. Subsequently, the culture plates were placed in an incubator for a period of 24 h. The MTT assay was conducted on days 1, 3, and 7 of the MG-63 cell culture. Following the designated time points, the scaffolds were washed twice with PBS solution. The culture plates were then incubated for 4 h, after which the formazan crystals were dissolved in a DMSO solution. To ensure homogeneity of the solution, the plates were subjected to agitation on a shaker for 15 min. Ultimately, the absorbance at 545 nm was determined using an ELISA system (STAT FAX 2100, USA).

Initially, sterilized samples were positioned in 24-well cell culture plates to facilitate cell adhesion. Subsequently, a cell suspension containing 30,000 cells in a volume of 80 μL was introduced onto the

Table 1
Process parameters used to print the AK/MNT/PCL scaffolds in this work.

Feature	value
Nozzle diameter [μm]	400
Layer thickness [μm]	300
Nozzle temperature [°C]	110 - 120
Print speed [mm/s]	3
Temperature of the work surface [°C]	25

samples, followed by an incubation period of 4 h. Upon successful cell adhesion, approximately 10 % FBS was introduced to the culture plate containing the samples. After 1 day, the samples were extracted and subjected to a 30-second wash with PBS. Cell fixation was achieved using a 3 % glutaraldehyde solution, followed by refrigeration for 2 h. Subsequently, the fixative was removed, and the samples underwent two consecutive washes with various ethanol concentrations (50, 60, 70, 80, and 96 %) and distilled water. The assessment of cell adhesion was ultimately conducted through SEM analysis.

Alkaline phosphatase, a pivotal factor in gauging the activation of osteoblasts during bone regeneration, was evaluated in samples initially seeded with 1×10^4 cells. After 7 and 14 days, cells were detached from the sample surfaces using trypsin, and the amount of alkaline phosphatase released from the cells was quantified using an ELISA kit (Pars, Azmoun, Iran) on the specified days. All quantity data and the results were expressed as the average (mean ± SD) standard deviation. ANOVA analysis was applied to compare the outcomes with the statistical significance denoted as $*p < 0.05$, $**p < 0.01$, $***p < 0.001$ and $****p < 0.0001$.

3. Results and discussion

3.1. Thermal behaviour of MNT

Fig. 2 illustrates the thermal analysis results, which reveal distinct weight reductions attributed to specific temperature ranges. The initial weight reduction, occurring in the temperature interval of 133 °C to 172 °C, is attributed to the elimination of adsorbed water. Subsequently, a second weight reduction, observed in the range of 280 °C to 386 °C, is identified as the decomposition of magnesium nitrite. Additionally, the weight loss occurring between 571 °C and 576 °C is associated with the decomposition of calcium nitrite. It is worth noting that crystallization was observed at 900 °C, highlighting its interdependence [35].

3.2. Characteristics of MNT and Ak powders

Figs. 3(a) and 3(b) show the XRD patterns of the synthesized AK and MNT ceramics, respectively, under different thermal treatment conditions (1300 °C for 1 hour and 1000 °C for 2 h). The XRD patterns of AK exhibit a well-defined peak at $2\theta = 31.27°$, which is consistent with the characteristic peak of AK documented in the JCPDS reference card (96–900–6450). This observation highlights the successful synthesis of AK ceramics and provides valuable insights into their crystalline nature and phase composition.

The XRD patterns of the synthesized MNT ceramics reveal a distinctive peak at approximately 33°, a characteristic feature corresponding to standard MNT, as corroborated by the JCPDS reference card (96–900–1078).

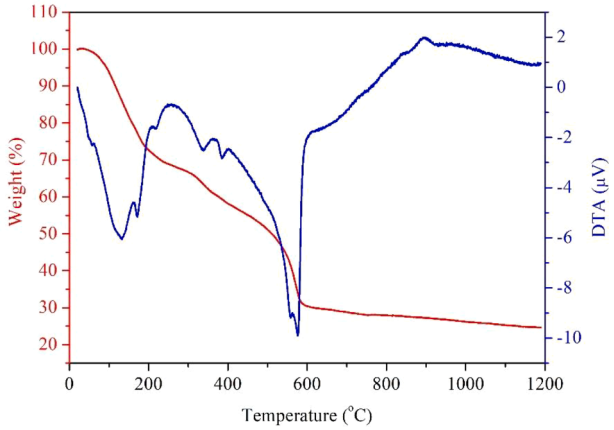

Fig. 2. STA curves of the synthesized MNT.

Additionally, three well-defined peaks were discerned at 2theta values of 24.59°, 33.76°, and 50.49°, indicative of MNT's orthorhombic crystal structure. Notably, the gel that sintered at 1000 °C exhibited impurities and diopside ($CaMgSi_2O_6$) alongside the presence of MNT. Figs. 3(c) and 3(d) illustrate the FTIR spectra of AK and MNT powders synthesized through the sol-gel method. The FTIR spectrum of AK showcases distinctive bands, such as the Ca=O group at approximately 589 cm^{-1}, O-Mg-O bending modes at around 473 cm^{-1}, and O-Si-O bands at 641 cm^{-1} and 680 cm^{-1}. Furthermore, Si-O stretching modes are evident at 848 cm^{-1}, 932 cm^{-1}, and 981 cm^{-1}. In the FTIR spectrum of MNT, stretching vibration modes of SiO_4 are observed in the range of 830–948 cm^{-1} and around 510 cm^{-1}, whereas the O-Mg-O bending mode is apparent at 486 cm^{-1} [36].

The existence of the Ca=O group is affirmed by the peak at 586 cm^{-1}, and the O-Si-O peak is identified at 640 cm^{-1}. Notably, Si-O stretching modes are evident at 974 cm^{-1}, while the bending vibration of H_2O is discernible at 1632 cm^{-1} [37]. The peak at 3423 cm^{-1} is attributed to moisture absorption. Figs. 3(e) and 3(f) depict the morphological characteristics of the synthesized powders using the sol-gel method. The inset of the TEM images provides a circular diameter distribution chart of the powders. The TEM micrographs reveal spherical shapes of both MNT and AK powders, with observable powder aggregation attributed to the high surface energy of these nanoparticles. The circular diameter chart inset in the TEM images indicates an average particle size of 47 nm for AK and 36 nm for MNT, respectively.

3.3. Structural characteristics of the scaffolds

Fig. 4 shows the SEM and energy-dispersive X-ray spectroscopy (EDS) map of the PCL and AK/MNT/PCL composite scaffolds. The scaffolds have a well-defined structure with regular interconnected pores, which allows for effective diffusion of oxygen and nutrients, promoting cell viability. The average pore size was measured to be 350 μm. The addition of ceramic nanoparticles to a polymer sample increases its viscosity, which in turn reduces its printing capabilities. To compensate for this, the printing pressure must be increased, resulting in thicker output fibers and smaller pores. The elemental image map of the scaffolds confirms the homogeneous dispersion of AK and MNT powders within the PCL matrix, highlighting the uniform distribution of components throughout the scaffold structure.

3.4. Mechanical properties of the scaffold

This investigation assessed the mechanical strength of scaffolds and identified the sample with superior properties for in vitro bioactivity and cellular studies. The samples with $10 \times 10 \times 10$ mm^3 were compressed with a speed of 1 mm/min due to the ASTM D695–15 (Standard Test method for Compressive Properties of Rigid Plastics) [38]. Fig. 5a shows stress-strain curves that illustrate the mechanical behaviors of scaffolds with different MNT/AK filler contents. The stress-strain profiles of PCL and PCL with 10 %, 15 %, and 20 % MNT-AK scaffolds exhibit distinct characteristics. The compressive strength values shown in Fig. 5b indicate that the PCL scaffold with 15 wt.% of AK/MNT nanopowders outperformed other configurations, with a value of 14.2 ± 0.84 MPa. Thus, the compressive strength of 15 % of samples is adequate for cancellous bone repair. The significant increase in compressive strength can be attributed to the inclusion of MNT, which is known for its mechanical robustness. However, microcracks were formed in 20 % of the samples due to agglomeration and increased stress concentration. Furthermore, it is noteworthy that Young's modulus of MNT closely approximates that of cortical bone (Young's modulus: 7–30 GPa) [39], highlighting its biomechanical significance. The compressive strength of PCL scaffolds was found to be 4.7 ± 1 MPa, which is considered insufficient for use in bone tissue engineering applications. A comparison analysis shows that the compressive strength of cancellous bone typically ranges from 2 to

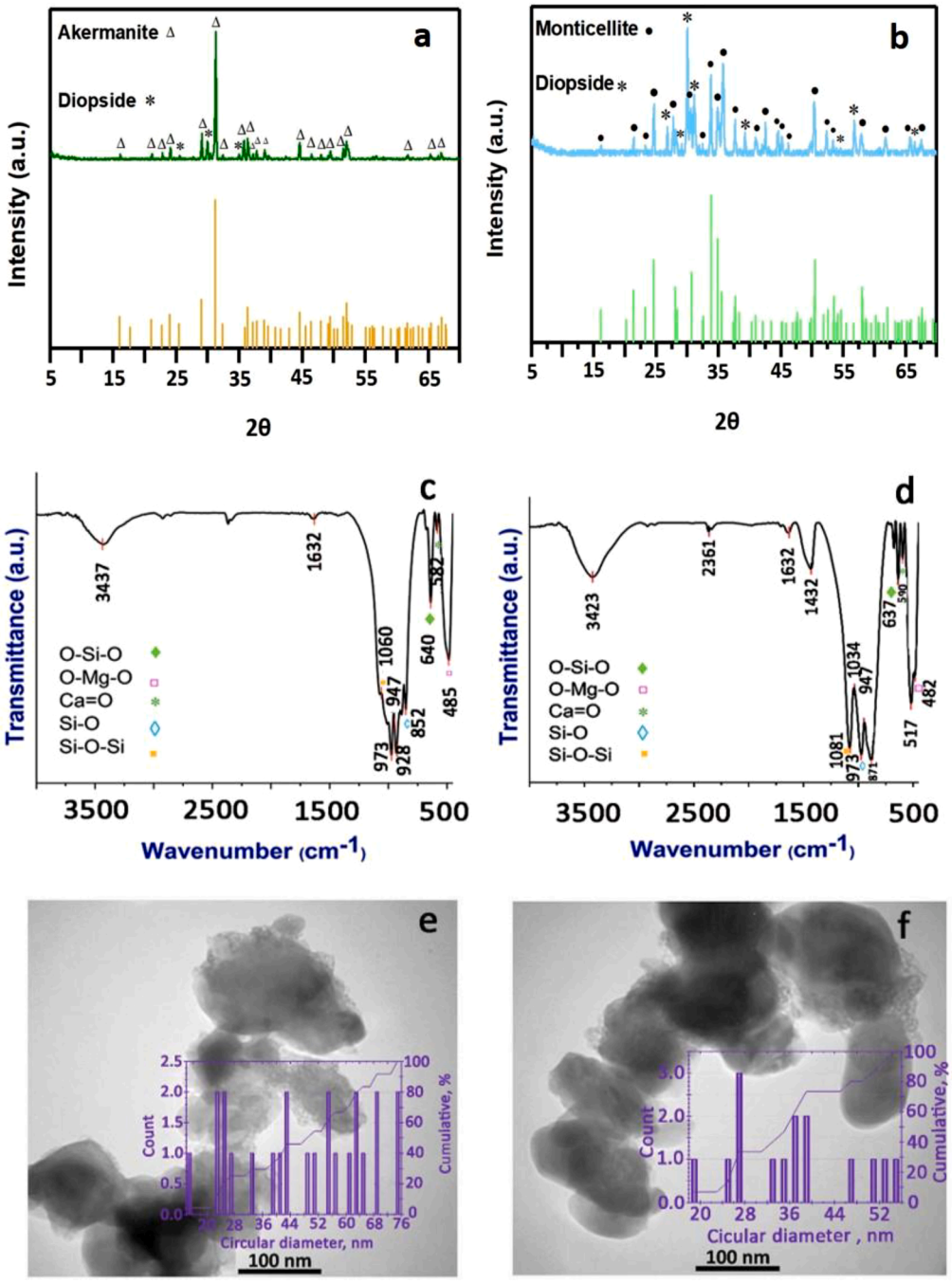

Fig. 3. (a-b) XRD patterns, (c-d) FTIR spectra, (e-f) TEM micrographs of AK and MNT.

20 MPa [40].

It is important to note that mechanical properties are closely related to porosity. Consequently, cortical bone, which has lower porosity, exhibits higher mechanical strength, whereas cancellous bone, with higher porosity, demonstrates relatively lower mechanical strength. This contrast highlights the trade-off between mechanical strength and the potential for cell growth and angiogenesis facilitated by increased porosity [41].

Based on these considerations, it is suggested that 3D-printed composite scaffolds possess mechanical properties suitable for their use in bone tissue engineering.

3.5. Bioactivity

The bioactivity of the scaffold was assessed by evaluating its ability to form apatite in a simulated body fluid (SBF) solution. Fig. 6 shows SEM images of the morphological changes of both the pure PCL scaffold and the AK/MNT/PCL scaffold after immersion in SBF for 7 and 28 days. No calcium phosphate precipitation was observed in the pure PCL scaffold, even after 7 and 28 days of immersion in SBF. The EDS patterns of the soaked PCL showed no presence of Ca and P elements, confirming the limited bioactivity of the pure PCL scaffold. In contrast, the AK/MNT/PCL scaffold exhibited a small amount of granular-shaped precipitate after 7 days of soaking, with more advanced precipitation observed after 28 days. This progress can be attributed to the increased formation of the calcium phosphate phase, particularly the apatite

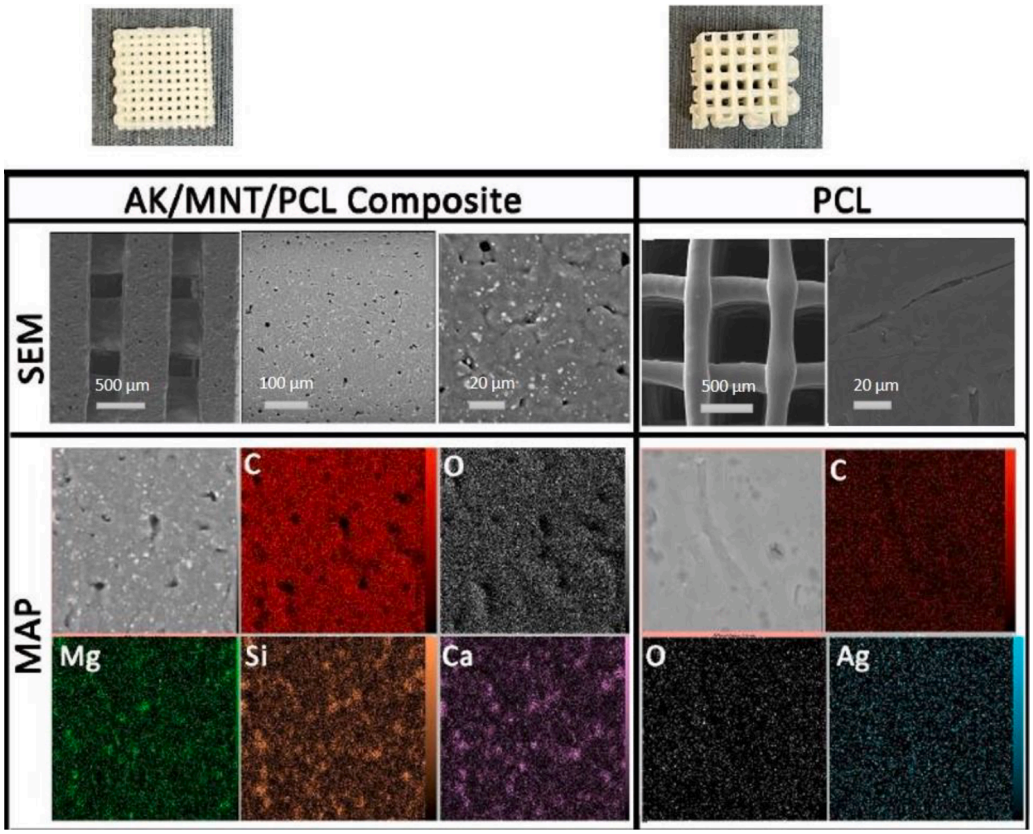

Fig. 4. SEM micrographs and EDS maps of the PCL and composite scaffold synthesized in this study.

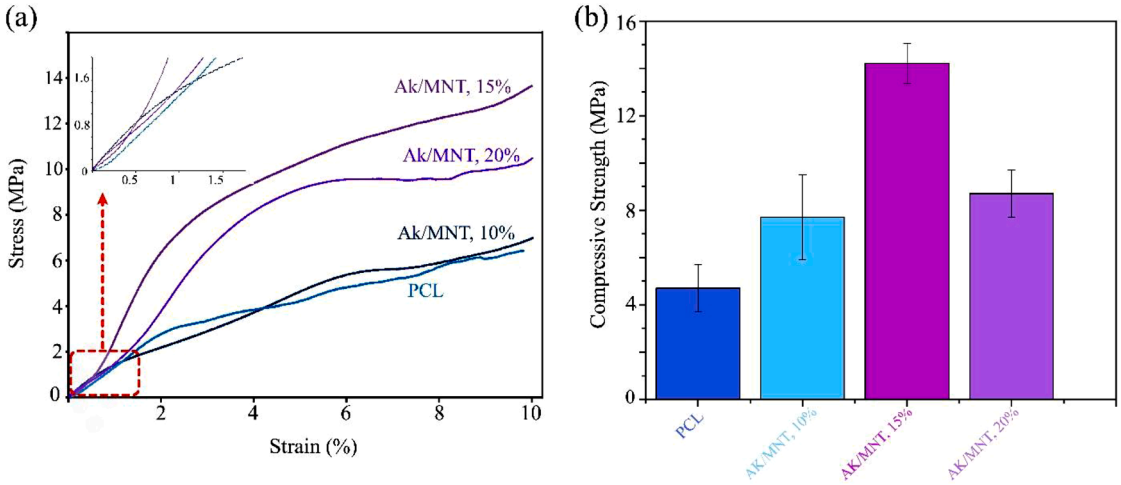

Fig. 5. The stress-strain curves (a) and compressive strength (b) of PCL and AK/MNT/PCL composite scaffolds.

phase. The study found that after 28 days, the ceramic in the composite scaffold was completely covered by spherical aggregates due to extended interaction with the SBF solution. The results suggest that silicate-based phases, such as AK and MNT, promote apatite formation. The study also acknowledges the importance of porous architecture in enhancing bioactivity and facilitating the release of ionic products. The bioceramics porous structure facilitates ion exchange with SBF, leading to faster dissolution and apatite formation [36].

In this analysis, EDS analysis was employed to ascertain the presence of calcium (Ca) and phosphorus (P). A comparative examination of the EDS patterns for the unsoaked (Fig. 4) and immersed composites (Fig. 6) scaffolds underscores the discernible alteration in surface chemistry following immersion. Specifically, prior to immersion, the EDS patterns revealed the most intense peak for silicon (Si), whereas post-immersion, calcium (Ca) emerged as the predominant element on the scaffold surface. This marked shift in elemental composition aligns with prior research, indicating that the precipitation of a bone-like apatite layer on biomaterial surfaces serves as a key indicator of bioactivity and contributes to enhanced in-vitro bone reconstruction [42].

The findings of this study support the effectiveness of AK and MNT in providing bioactive properties to PCL-based tissue scaffolds.

Fig. 7 presents a comparative analysis of the FTIR spectra of the composite scaffold before (Fig. 7a) and after (Fig. 7b) immersion in the SBF solution for 28 days. The FTIR spectra exhibit distinct bands

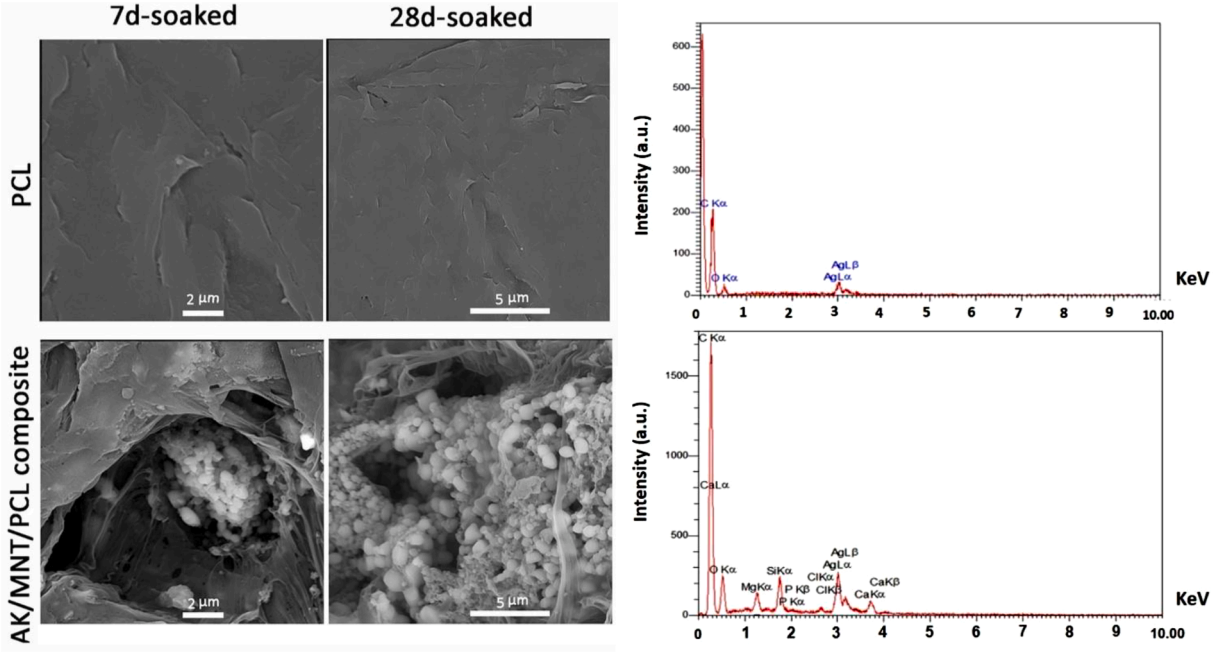

Fig. 6. The SEM and EDS analyses of the PCL and AK/MNT/PCL scaffolds after immersion in SBF solution.

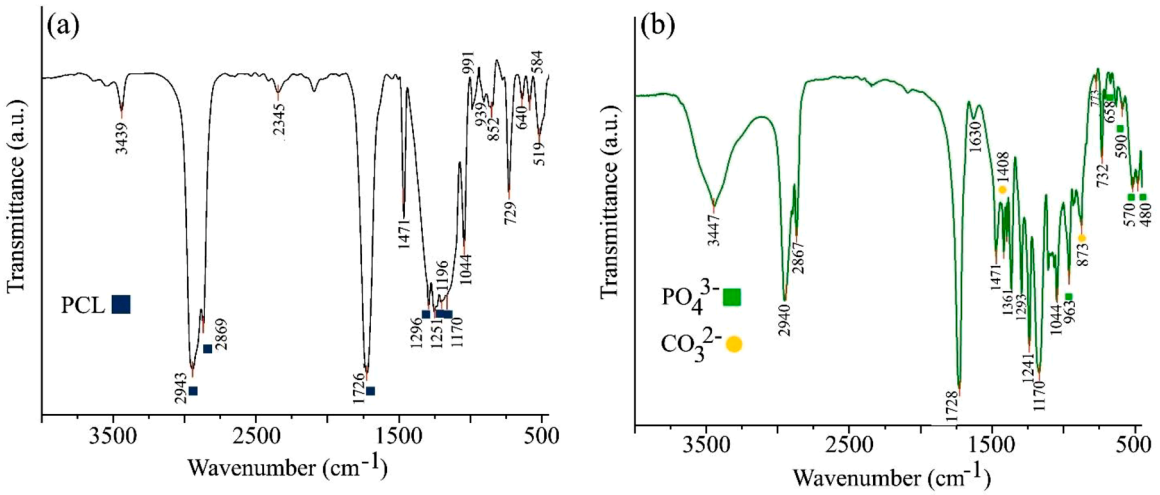

Fig. 7. FTIR of AK/MNT/PCL scaffold before (a) and after (b) 28 days immersion in SBF solution.

attributed to PCL at 2865 cm^{-1} (symmetric CH2 stretching), 1240 cm^{-1} (asymmetric COC stretching), and 1727 cm^{-1} (carbonyl stretching) [43]. Notably, following 28 days of immersion in SBF, a new peak at approximately 1405 cm^{-1} emerges, signifying the presence of the carbonate group [36]. Additionally, broad bands in the range of 900–1300 cm^{-1} are attributed to PO_4^{3-}, with a distinctive band at 463 cm^{-1} indicative of phosphate ions. The vibration of the P-O mode is reflected in the band at 968 cm^{-1}, while the wide band at 3100–3500 cm^{-1} is associated with adsorbed water [18]. Furthermore, the absorption peak at 875 cm^{-1} is correlated with the carbonate group, and the complex absorption band in the range of 1400–1500 cm^{-1} signifies the presence of carbonates [44].

This spectral analysis provides valuable insights into the chemical transformations occurring in the composite scaffold during immersion, corroborating the scaffold's interaction with the SBF solution and the subsequent development of carbonate and phosphate species on the scaffold surface.

3.6. Cell cytotoxicity, cell attachment and ALP activity

To assess cytotoxicity, the MTT assay was conducted on control samples, PCL, and AK/MN/PCL scaffolds at intervals of days 1, 3, and 7. The results, illustrated in Fig. 8, reveal consistently high cell viability across all samples. Importantly, none of the samples exhibited any indications of cytotoxicity. Notably, AK/MN/PCL scaffolds demonstrated superior cell viability compared to other scaffold variants. Furthermore, in comparison with both PCL scaffolds and other reference studies involving β-tricalcium phosphate, AK and MNT exhibited a noteworthy positive effect on cell behaviour, surpassing the performance of the control sample [45].

These findings underscore the non-cytotoxic nature of the scaffolds and highlight the favourable impact of AK and MNT on cellular responses, positioning them as promising elements for enhancing the biocompatibility of tissue scaffolds. Fig. 8 illustrates the ALP activity of three distinct scaffold types on days 7 and 14. Notably, the ALP activity in AK/MN/PCL scaffolds significantly surpasses that observed in the

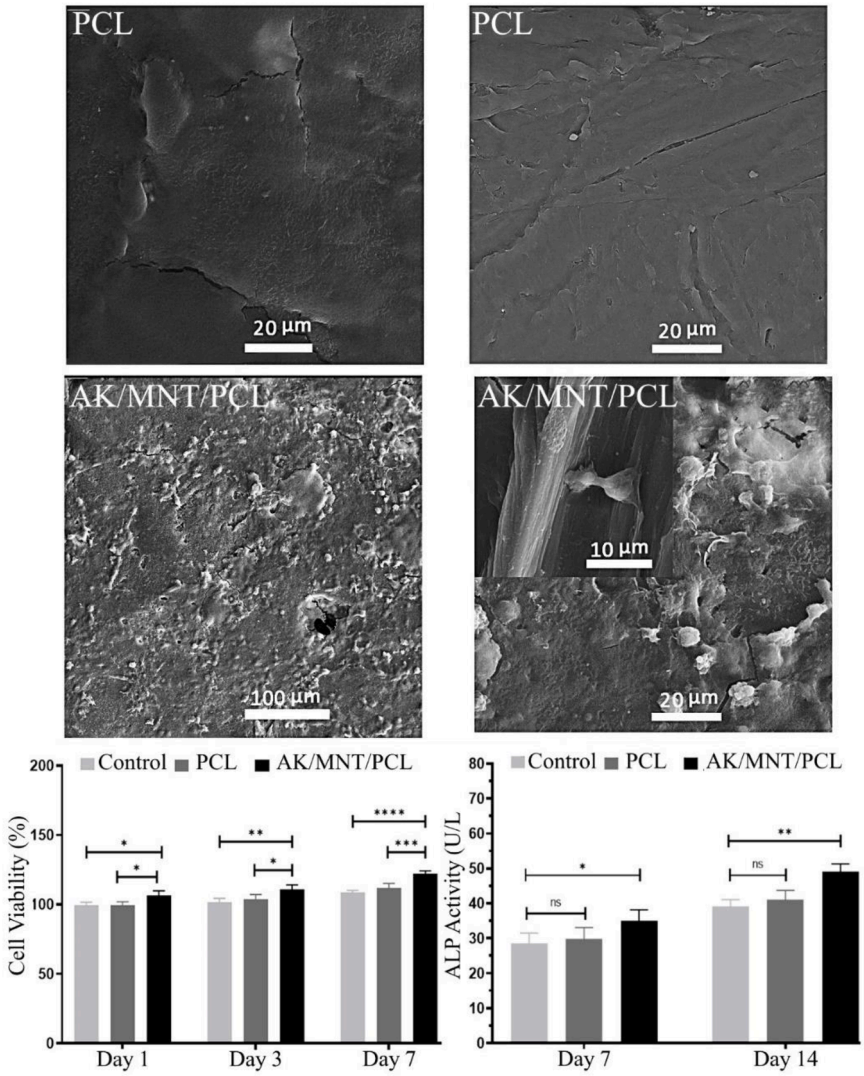

Fig. 8. Cell attachment, cell viability and ALP activity of MG63 cells on the scaffolds.

other samples. As a benchmark, a control comprising a well with culture medium and cells was incorporated for reference. The ALP activity of cells demonstrated a notable increase with the presence of MNT and AK content in the composite scaffolds compared to PCL scaffolds ($p < 0.05$). This finding signifies a substantial positive impact on the osteogenic differentiation of cells within the AK/MN/PCL scaffold, suggesting its potential as a favourable environment for promoting bone-related cellular activities.

Cell attachment was assessed to evaluate the adhesion of MG-63 cells onto the composite scaffolds. Cells were cultivated on the scaffolds for 2 days. Notably, the cellular morphology exhibited predominantly spherical shapes. Analysis of SEM images revealed that the structure of the composite scaffolds facilitated favourable cell adhesion. Particularly, cells on the AK-MNT/PCL scaffolds displayed an extended cytoplasmic membrane and higher cell density. Conversely, the SEM images indicated that PCL scaffolds were inadequate for promoting cell attachment. The role of AK in influencing the growth and proliferation of MG-63 cells emerged as a significant factor based on the observed cellular behaviours [46].

4. Conclusion

The AK and MNT were successfully synthesized using the sol-gel method, a precise technique for nanopowder fabrication. The resulting scaffolds have interconnected pores and were carefully crafted using the Fused Deposition Modeling 3D printing approach. This scaffold architecture shows promise in various applications, particularly in tissue engineering. The presence of pores creates an environment that promotes optimal cell growth and proliferation. Additionally, the interconnected pores facilitate the uniform distribution of essential substances, such as nutrients and vascular ingrowth, throughout the scaffold structure. The scaffolds have a well-defined structure with regular interconnected pores, and the average pore size was measured to be 350 µm. The incorporation of ceramic nanoparticles into a polymer sample results in an increase in viscosity, leading to a reduction in its printing capabilities. The stress-strain curves, which illustrate the mechanical behavior of scaffolds with different MNT/AK filler contents, indicate that the PCL scaffold with 15 wt.% of AK/MNT nanopowders outperformed other configurations, with a value of 14.2 ± 0.84 MPa. Thus, the compressive strength of 15 % of samples is adequate for cancellous bone repair. In addition to mechanical considerations, AK and MNT nanopowders also affected the scaffold's ability to form apatite, which is a crucial factor in bone tissue engineering. Comprehensive studies on cell behavior have shown that introducing AK and MNT nanopowders into the PCL scaffold positively impacts cell attachment, viability, and ALP activity. Combining AK and monticellite nanopowders with PCL to improve bioactivity and mechanical strength has not worked yet. However, it is important to note that further

investigations, particularly in vivo and human clinical studies, are necessary to substantiate their therapeutic efficacy and safety profile. AK/MN/PCL scaffolds demonstrated superior cell viability compared to other scaffold variants.

Declaration of competing interest

The authors declare that they have no known competing financial interests or personal relationships that could have appeared to influence the work reported in this paper.

References

[1] P.S.C. Rinaldo Florencio-Silva, Gisela Rodrigues da Silva Sasso, Estela Sasso-Cerri, Manuel Jesus Simões, Physiology of bone tissue, Immuno-anal. Biol. Spécial. 7 (6) (2015) 17–24.

[2] W. Wang, K.W.K. Yeung, Bone grafts and biomaterials substitutes for bone defect repair: a review, Bioact. Mater. 2 (4) (2017) 224–247, https://doi.org/10.1016/j.bioactmat.2017.05.007.

[3] T. Tariverdian, F. Sefat, M. Gelinsky, M. Mozafari, Scaffold For Bone Tissue Engineering, Elsevier Ltd, 2019, https://doi.org/10.1016/B978-0-08-102563-5.00010-1.

[4] M. Qasim, D.S. Chae, N.Y. Lee, Bioengineering strategies for bone and cartilage tissue regeneration using growth factors and stem cells, J. Biomed. Mater. Res. - Part A 108 (3) (2020) 394–411, https://doi.org/10.1002/jbm.a.36817.

[5] A. Liu, et al., Three-dimensional printing akermanite porous scaffolds for load-bearing bone defect repair: an investigation of osteogenic capability and mechanical evolution, J. Biomater. Appl. 31 (5) (2016) 650–660, https://doi.org/10.1177/0885328216664839.

[6] M. Díaz-Pérez, L. Grima, B.M. Moshtaghioun, J.I. Peña, CaO–MgO–SiO2–P2O5-based multiphase bio-ceramics fabricated by directional solidification: microstructure features and in vitro bioactivity studies, Ceram. Int. 47 (12) (2021) 17041–17048, https://doi.org/10.1016/j.ceramint.2021.03.011.

[7] Y. Huang, et al., In vitro and in vivo evaluation of akermanite bioceramics for bone regeneration, Biomaterials 30 (28) (2009) 5041–5048, https://doi.org/10.1016/j.biomaterials.2009.05.077.

[8] E. Askari, S.M. Naghib, A. Seyfoori, M.A. Javidi, A. Madjid Ansari, Highly bioactive Akermanite-Monticellite nanocomposites for bone tissue engineering: a tunable three-dimensional biological study, J. Mater. Res. Technol. 20 (2022) 4066–4076, https://doi.org/10.1016/j.jmrt.2022.08.136.

[9] Ş. Duman, B. Bulut, Effect of akermanite powders on mechanical properties and bioactivity of chitosan-based scaffolds produced by 3D-bioprinting, Ceram. Int. 47 (10) (2021) 13912–13921, https://doi.org/10.1016/j.ceramint.2021.01.258.

[10] X. Chen, J. Ou, Y. Wei, Z. Huang, Y. Kang, G. Yin, Effect of MgO contents on the mechanical properties and biological performances of bioceramics in the MgO-CaO-SiO2 system, J. Mater. Sci. Mater. Med. 21 (5) (2010) 1463–1471, https://doi.org/10.1007/s10856-010-4025-5.

[11] H. Mohammadi, Y.M.B. Ismail, K.A. Shariff, A.F.M. Noor, Effect of substitutional strontium on mechanical properties of akermanite ceramic prepared by solid-state sintering, Mater. Today Proc. 17 (2019) 929–936, https://doi.org/10.1016/j.matpr.2019.06.393.

[12] R.A. Youness, D.M. Tag El-deen, M.A. Taha, A review on Calcium Silicate ceramics: properties, limitations, and solutions for their use in biomedical applications, Silicon 15 (6) (2023) 2493–2505, https://doi.org/10.1007/s12633-022-02207-3.

[13] A. Zare-Harofteh, S. Saber-Samandari, S. Saber-Samandari, The effective role of akermanite on the apatite-forming ability of gelatin scaffold as a bone graft substitute, Ceram. Int. 42 (15) (2016) 17781–17791, https://doi.org/10.1016/j.ceramint.2016.08.106.

[14] X. Dong, et al., Investigation of the mechanical properties of a bony scaffold for comminuted distal radial fractures: addition of akermanite nanoparticles and using a freeze-drying technique, J. Mech. Behav. Biomed. Mater. 121 (April) (2021) 104643, https://doi.org/10.1016/j.jmbbm.2021.104643.

[15] H. Mohammadi, et al., Bioinorganics in bioactive calcium silicate ceramics for bone tissue repair: bioactivity and biological properties, J. Ceram. Sci. Technol. 5 (1) (2014) 1–12, https://doi.org/10.4416/JCST2013-00027.

[16] M. Parashar, V.K. Shukla, R. Singh, Metal oxides nanoparticles via sol–gel method: a review on synthesis, characterization and applications, J. Mater. Sci. Mater. Elect. 31 (5) (2020) 3729–3749, https://doi.org/10.1007/s10854-020-02994-8.

[17] A.H. Aghajanian, A. Bigham, M. Khodaei, S. Hossein Kelishadi, Porous titanium scaffold coated using forsterite/poly-3-hydroxybutyrate composite for bone tissue engineering, Surf. Coat. Technol. 378 (July) (2019) 124942, https://doi.org/10.1016/j.surfcoat.2019.124942.

[18] E. Kalantari, S. Morteza Naghib, M. Reza Naimi-Jamal, R. Esmaeili, keivan Majidzadeh-A, and M. Mozafari, "Nanostructured monticellite: an emerging player in tissue engineering," 2018. [Online]. Available: www.sciencedirect.comwww.materialstoday.com/proceedings2214-7853.

[19] X. Hou, G. Yin, X. Chen, X. Liao, Y. Yao, Z. Huang, Effect of akermanite morphology on precipitation of bone-like apatite, Appl. Surf. Sci. 257 (8) (2011) 3417–3422, https://doi.org/10.1016/j.apsusc.2010.11.037.

[20] C. Wu, J. Chang, Synthesis and apatite-formation ability of akermanite, Mater. Lett. 58 (19) (2004) 2415–2417, https://doi.org/10.1016/j.matlet.2004.02.039.

[21] M.H.V.F.I.K. Mihailova, L. Radev, V.A. Aleksandrova, I.V. Colova, I.M.M. Salvado, Novel merwinite/akermanite ceramics: in vitro bioactivity, Bulg. Chem. Commun. 47 (1) (2015) 253–260.

[22] C. Wu, J. Chang, A review of bioactive silicate ceramics, Biomed. Mater. 8 (3) (2013), https://doi.org/10.1088/1748-6041/8/3/032001.

[23] G. Ratheesh, J.R. Venugopal, A. Chinappan, H. Ezhilarasu, A. Sadiq, S. Ramakrishna, 3D fabrication of polymeric scaffolds for regenerative therapy, ACS Biomater. Sci. Eng. 3 (7) (2017) 1175–1194, https://doi.org/10.1021/acsbiomaterials.6b00370.

[24] A. Farazin, F. Aghadavoudi, M. Motififard, S. Saber-Samandari, A. Khandan, Nanostructure, molecular dynamics simulation and mechanical performance of PCL membranes reinforced with antibacterial nanoparticles, J. Appl. Comput. Mech. 7 (4) (2021) 1907–1915, https://doi.org/10.22055/JACM.2020.32902.2097.

[25] A. Prasad, B. Kandasubramanian, Fused deposition processing polycaprolactone of composites for biomedical applications, Polym. Technol. Mater. 58 (13) (2019) 1365–1398, https://doi.org/10.1080/25740881.2018.1563117.

[26] X. Yang, Y. Wang, Y. Zhou, J. Chen, Q. Wan, The application of polycaprolactone in three-dimensional printing scaffolds for bone tissue engineering, Polymers (Basel) 13 (16) (2021), https://doi.org/10.3390/polym13162754.

[27] M. Mohammadi, et al., Robocasting of single and multi-functional calcium phosphate scaffolds and its hybridization with conventional techniques: design, fabrication and characterization, Appl. Sci. 10 (23) (2020) 1–22, https://doi.org/10.3390/app10238677.

[28] A. Khademhosseini, R. Langer, A decade of progress in tissue engineering, Nat. Protoc. 11 (10) (2016) 1775–1781, https://doi.org/10.1038/nprot.2016.123.

[29] S. Zhang, S. Vijayavenkataraman, W.F. Lu, J.Y.H. Fuh, A review on the use of computational methods to characterize, design, and optimize tissue engineering scaffolds, with a potential in 3D printing fabrication, J. Biomed. Mater. Res. - Part B Appl. Biomater. 107 (5) (2019) 1329–1351, https://doi.org/10.1002/jbm.b.34226.

[30] W.J. Choi, et al., Rapid development of dual porous poly(lactic acid) foam using fused deposition modeling (FDM) 3D printing for medical scaffold application, Mater. Sci. Eng. C 110 (September 2019) (2020) 110693, https://doi.org/10.1016/j.msec.2020.110693.

[31] R. Ranjan, D. Kumar, M. Kundu, S. Chandra Moi, A critical review on classification of materials used in 3D printing process, Mater. Today Proc. 61 (2) (2022) 43–49, https://doi.org/10.1016/j.matpr.2022.03.308.

[32] V. Melčová, et al., Fdm 3d printed composites for bone tissue engineering based on plasticized poly(3-hydroxybutyrate)/poly(d,l-lactide) blends, Polymers. (Basel) 12 (12) (2020) 1–19, https://doi.org/10.3390/polym12122806.

[33] A.S. Alagoz, V. Hasirci, 3D printing of polymeric tissue engineering scaffolds using open-source fused deposition modeling, Emergent. Mater. 3 (4) (2020) 429–439, https://doi.org/10.1007/s42247-019-00048-2.

[34] Y. Zou, J. Malzbender, Development and optimization of porosity measurement techniques, Ceram. Int. 42 (2) (2016) 2861–2870, https://doi.org/10.1016/j.ceramint.2015.11.015.

[35] E. Askari, et al., A hybrid approach for in-situ synthesis of bioceramic nanocomposites to adjust the physicochemical and biological characteristics, J. Mater. Res. Technol. 14 (2021) 464–474, https://doi.org/10.1016/j.jmrt.2021.06.063.

[36] A.K. Sharafabadi, M. Abdellahi, A. Kazemi, A. Khandan, N. Ozada, A novel and economical route for synthesizing akermanite (Ca2MgSi2O7) nano-bioceramic, Mater. Sci. Eng. C 71 (Feb. 2017) 1072–1078, https://doi.org/10.1016/J.MSEC.2016.11.021.

[37] R. Choudhary, S. Koppala, S. Swamiappan, Bioactivity studies of calcium magnesium silicate prepared from eggshell waste by sol-gel combustion synthesis, J. Asian Ceram. Soc. 3 (2) (2015) 173–177, https://doi.org/10.1016/j.jascer.2015.01.002.

[38] C.G. Simon, M.J. Yaszemski, A. Ratcliffe, P. Tomlins, R. Luginbuehl, J.A. Tesk, ASTM international workshop on standards and measurements for tissue engineering scaffolds, J. Biomed. Mater. Res. - Part B Appl. Biomater. 103 (5) (2015) 949–959, https://doi.org/10.1002/jbm.b.33286.

[39] X. Chen, et al., Synthesis and characteristics of monticellite bioactive ceramic, J. Mater. Sci. Mater. Med. 19 (3) (Mar. 2008) 1257–1263, https://doi.org/10.1007/s10856-007-3233-0.

[40] S. Bose, M. Roy, A. Bandyopadhyay, Recent advances in bone tissue engineering scaffolds, Trends Biotechnol 30 (10) (2012) 546–554, https://doi.org/10.1016/j.tibtech.2012.07.005.

[41] S. Wu, X. Liu, K.W.K. Yeung, C. Liu, X. Yang, Biomimetic porous scaffolds for bone tissue engineering, Mater. Sci. Eng. R Rep. 80 (1) (2014) 1–36, https://doi.org/10.1016/j.mser.2014.04.001.

[42] L. Chen, D. Zhai, C. Wu, J. Chang, Poly(d, ʟ-lactic)-reinforced akermanite bioceramic scaffolds: preparation and characterization, Ceram. Int. 40 (8 PART B) (2014) 12765–12775, https://doi.org/10.1016/j.ceramint.2014.04.130.

[43] L. Ghasemi-mobarakeh, M.P. Prabhakaran, M. Morshed, Bio-functionalized PCL nano fi brous scaffolds for nerve tissue engineering, Mater. Sci. Eng. C 30 (8) (2010) 1129–1136, https://doi.org/10.1016/j.msec.2010.06.004.

[44] I.K. Mihailova and L.N. Radev, "Åkermanite based bioactive ceramics : structural and in-vitro bioactivity characterization," vol. 50, pp. 135–142, 2018.
[45] M. Arastouei, M. Khodaei, S.M. Atyabi, M. Jafari Nodoushan, The in-vitro biological properties of 3D printed poly lactic acid/akermanite composite porous scaffold for bone tissue engineering, Mater. Today Commun. 27 (January) (2021) 102176, https://doi.org/10.1016/j.mtcomm.2021.102176.
[46] L. Xia, et al., Akermanite bioceramics promote osteogenesis, angiogenesis and suppress osteoclastogenesis for osteoporotic bone regeneration, Sci. Rep. 6 (September 2015) (2016) 1–17, https://doi.org/10.1038/srep22005.